Citation: Ignacio Cuiral-Zueco, Yiannis Karayiannidis, and Gonzalo López-Nicolás. Contour based object-compliant shape control. IEEE Robotics and Automation Letters, 8(8):5164–5171, 2023.

Contour based object-compliant shape control

Ignacio Cuiral-Zueco, Yiannis Karayiannidis and Gonzalo López-Nicolás

***Abstract*—Shape control strategies seek to bring deformable objects towards a desired target shape. However, conventional methods focus on reaching the target shape without considering the extent to which the object is deformed during the control process. Control actions may generate unnecessary deformations and thus increase the possibility of object over-stressing and failure. In this paper we tackle the problem of vision-based object-compliant shape control (OCSC) with focus on 2D contours of texture-less objects. We propose a novel shape control framework that makes use of a multi-scale analysis of the contour's length and curvature to reduce the amount of deformation objects need to undergo during the shape control task. We evaluate our approach with simulations and experiments.**

***Index Terms*—Visual servoing, multi-robot systems, shape control, perception for grasping and manipulation.**

I. Introduction

SHAPE control is required in multiple applications such as industrial processes or domestic robotics [1] [2], where preserving the object's integrity can be a critical aspect for the success of the manipulation task. Explicitly considering and analysing the extent to which an object is deformed during a shape control task constitutes an important challenge. The amount of deformation the object undergoes may be disregarded when the object allows for a large range of deformations. However, we believe that avoiding unnecessary deformations is a more reliable approach. One may suggest the use of mechanical sensors (e.g. strain gauges, torque sensors) in order to avoid reaching mechanical limits of the object (e.g. elastic limit). However, the use of mechanical sensors relies on costly and/or object-invasive setups while not allowing full coverage of the object as positioning a large amount of mechanical sensors may be inconvenient in most applications. Therefore, we propose a vision-based object-compliant shape control (OCSC) framework to reduce the amount of deformation the object needs to undergo to acquire the target shape (see Fig. 1).

A. Related work

Some approaches in the vision-based shape control literature, without focus on OCSC, use a reduced number of shape features (such as feature points or segments) in order to perform the shape control task (e.g., [3], [4]). This can be of use in certain applications, however, in these frameworks, features are *blind* to object parts that are not within their range of description and thus they are not suitable for OCSC, where a holistic analysis considers all of the object parts. Methods such as those presented in [5], [6] or [7] analyse the object's shape in a global manner through its 2D visible silhouette and the use of homogeneous contour mappings; they are purely based on extrinsic errors[1]. However, despite globally sampling the object's geometry, some control methods require filtering the shape's information (e.g., [5], based on Principal Component Analysis). Such methods might be disregarding local yet critical deformation processes through filtering. We therefore focus on analysis like those proposed in [6], based on point-to-point error, or [7], based on frequency domain error, as they provide a holistic error definition where filtering is not necessarily required from a theoretical standpoint.

Some characteristic examples of point-to-point (P2P) and frequency domain defined shape errors (or shape energies) are presented in [6] and [7]. Other methods tackle the shape error reduction defined by such energies while also incorporating additional terms that consider deformation cost. In particular, [9], [10] and [11] aim at reducing the P2P energy along with deformation costs associated to the object's strain. Deformation costs in [9] and [10] are based on the comparison of Euclidean point distances with respect to the geodesic distances between the at-rest object points. This deformation cost can be calculated directly in simulated processes where point correspondences between object states are known. However, in a real setup, such cost requires a mapping between object states. Method in [10], rather than computing a mapping, approximates the derivative of the strain cost with the miss-alignment (i.e., cosine value) between the gripper's velocity vectors and the tangent vector (at the gripper's position) to the geodesic paths defined between pairs of grippers. This

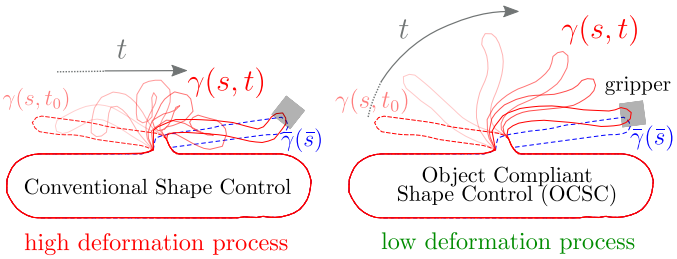

Fig. 1. Comparison of two different solutions for the same shape control problem. The first one only considers extrinsic error between contour points whereas the second one defines the shape error through our proposed shape metric, resulting in a more object-compliant process (elements of the figure introduced in section I-C).

Manuscript received March 10, 2023; Accepted June 23, 2023. This paper was recommended for publication by Editor P. Vasseur upon evaluation of the Associate Editor and Reviewers' comments. This work was supported via projects PID2021-124137OB-I00 and TED2021-130224B-I00 funded by MCIN/AEI/10.13039/501100011033, by ERDF A way of making Europe and by the European Union NextGenerationEU/PRTR. This work was also partially supported by the Wallenberg AI, Autonomous Systems and Software Program (WASP) funded by the Knut and Alice Wallenberg Foundation.

I. Cuiral-Zueco and G. López-Nicolás are with Instituto de Investigación en Ingeniería de Aragón, Universidad de Zaragoza, Spain, ignaciocuiral@unizar.es, gonlopez@unizar.es.

Y. Karayiannidis is with Department of Automatic Control, Lund University, and is a member of the ELLIIT Strategic Research Area, yiannis@control.lth.se.

[1]See [8] for a definition of *extrinsic* in the context of shape analysis.

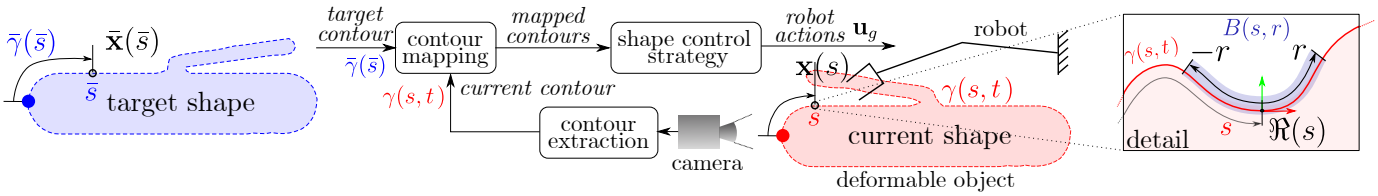

Fig. 2. Illustration of the problem setup and general shape control scheme. Object surfaces constitute the current and target shapes through their parameterised contour curves $\gamma(s,t), \bar{\gamma}(\bar{s})$, with extrinsic representation through 2D coordinates $\mathbf{x}(s)$, $\bar{\mathbf{x}}(\bar{s})$. A contour map between $\gamma(s,t)$ and $\bar{\gamma}(\bar{s})$ is computed, serving as input for the shape control strategy that defines robot actions $\mathbf{u}_g$ to be applied to the object. In this paper, we use Jacobian-based shape energy minimisation as shape control strategy. At each contour point s, a local reference $\Re(s)$ is defined through the tangent and normal vectors at s (see the detail at the right), where a geodesic ball $B(s,r)$ of radius r is shown.

approximation assumes pure tensile stress along geodesics between grippers and deformations around the grippers to be representative of deformations on the whole object. Another geodesic-distance based deformation cost is proposed in [11], where the variations on local distance between landmark points are considered. Similarly to [9], [11] relies on tracking specific object points and disregards bending stress and deformations that do not significantly change geodesic distances.

A challenging problem regarding vision-based OCSC is the definition of a holistic shape metric that, without depending on the object's texture, allows to generate low deformations between object states (rather than relying on additional deformation costs and/or constraints). Deformation costs and constraints can be used as support for such metric. However, neither the shape metric nor the additional constraints/costs should disregard changes in curvature: pronounced changes in curvature imply large bending stress while not producing significant changes on the object's geodesic distances.

B. Object-compliant method overview

In this paper we present a vision-based OCSC framework for deformable objects that lack visual texture (i.e., objects whose surface points cannot be tracked). Other approaches that tackle OCSC either rely on objects with rich texture (e.g., [9], [11]) or confine their analysis to the object regions that are close to the grippers (e.g., [10]). Our proposed method analyses the visible contour of the object in order to quantify the amount of deformation it undergoes. We focus on shape control processes involving slow and isotropic deformations that allow to disregard inertia. The main contributions of this paper are:

- A geometry-based deformation energy that constitutes a shape metric. Such metric considers the object's geometric features in a multi-scale level and thus allows to quantify deformations in a holistic manner. Furthermore, when directly used as shape control error, the proposed metric inherently leads to more object-compliant behaviours than other conventional metrics (e.g., metrics as in [6] or [7]). We validate our shape metric as a deformation measure and as an object-compliant energy through comparisons in simulations and experiments.
- An OCSC framework that extends the use of the proposed shape metric and allows to introduce deformation costs and constraints considering both changes in length (i.e., tensile and compression stress) and curvature (i.e., bending stress) of texture-less objects. In the literature, approaches such as [9], [10] or [11] consider excessive stretching but disregard deformations induced by pure compression or bending.

The proposed object-compliant metric is introduced in section II. We develop on the OCSC framework in section III. The performance of the framework is illustrated in section IV, where we present comparative experiments using a dual-arm manipulator (see the attached **video**).

C. Problem setup

Consider 2D visual contour data extracted from video frames (see Fig. 2), that is a curve $\gamma(s,t)$, parameterised by $s \in \mathbb{R}$, obtained from the texture-less object being manipulated. Similarly, one can define the fixed target shape through a curve $\bar{\gamma}(\bar{s})$, parameterised by $\bar{s} \in \mathbb{R}$. Contour points have extrinsic global coordinates $\mathbf{x}(s), \bar{\mathbf{x}}(\bar{s}) \in \mathbb{R}^2$. We define local frames of reference $\Re(s), \bar{\Re}(\bar{s})$ on $\gamma(s), \bar{\gamma}(\bar{s})$ with orthogonal axes in the tangent and the normal space. The object is grasped by robotic grippers for which we assume proper grasping stability. Grippers g do not need to be visible or placed along the contour, they are modelled with single integrator dynamics and perform 3 DoF actions $\mathbf{u}_g \in \mathbb{R}^2 \times S^1$ (2 translations and 1 rotation).

II. Geometry-based deformation energy

A. Proposed multi-scale normal (MSN) energy: E_{MSN}

In this section we present a geometry-based deformation energy for OCSC. In texture-less objects, the only visual indicators of objects undergoing deformations are the local changes in length and curvature of their contour. We therefore define our analysis using these two key elements.

Our proposed energy relies on a shape representation analogous to the discrete multi-scale Laplacian descriptors presented in [12] for elastic contour mapping. We define a continuous multi-scale normal (MSN) shape representation that provides a notion of *multi-scale mean curvature*. We make use of geodesic balls $B(s,r) \subseteq \gamma(s)$ centred at s with radius $r \in (0, r_{\max}] \subset \mathbb{R}$, (Fig. 2), being $r_{\max} = l(t)/2$ and $l(t) \in \mathbb{R}$ the total contour length. In this paper we will refer to radius r as scale of analysis (or simply *scale*). A scale defines the neighbouring region (i.e., the scope of analysis) at a given point s. Therefore, our proposed shape representation $\mathbf{l}(s,r) \in \mathbb{R}^2$ is obtained as

$$\mathbf{l}(s,r) = -\frac{1}{r}\int_{B(s,r)} \mathbf{x}^{\Re(s)}(s')\mathrm{d}l, \tag{1}$$

where $\mathbf{x}^{\Re(s)}(s') = (x^{\Re(s)}(s'), y^{\Re(s)}(s'))^\intercal \in \mathbb{R}^2$ are the extrinsic position vectors of points corresponding to parameter values $s' \in B(s,r)$ and expressed in the reference $\Re(s)$. Element $\mathrm{d}l$ in (1) is the differential element of contour length $l(t)$. As $r \to 0$, (1) leads to the curvature weighted normal vectors (referred to $\Re(s)$). Coordinates of points within the integration domain are still expressed from frame $\Re(s) \not\equiv \Re(s')$ and, therefore, descriptors $\mathbf{l}(s,r)$ constitute both intrinsic and extrinsic descriptors [8].

Consider $\bar{s} = \Pi(s,t)$ where $\Pi(s,t) : \gamma(t) \to \bar{\gamma}$ is an elastic map (diffeomorphism) that maximises multi-scale curvature similarity between contours. Using the shape representation (1), we define shape error $\mathbf{e}_{\mathrm{MSN}}$ as

$$\mathbf{e}_{\mathrm{MSN}}(s,r,t) = \mathbf{l}(s,r,t) - \bar{\mathbf{l}}(\Pi(s,t),r), \tag{2}$$

where $\bar{\mathbf{l}}(\Pi(s,t),r)$ constitutes the multi-scale normal (MSN) descriptor of the target shape at point $\Pi(s,t) = \bar{s}$. Using error (2) we introduce our proposed geometry-based deformation energy as:

$$E_{\mathrm{MSN}}(\gamma(t),\bar{\gamma}) = \min_{\Pi} \int_0^{l(t)} \int_0^{r_{\max}} \mathbf{e}_{\mathrm{MSN}}^\intercal \mathbf{e}_{\mathrm{MSN}} \mathrm{d}r\mathrm{d}s, \tag{3}$$

where $l(t)$ is the length of curve $\gamma(t)$. The optimisation process for obtaining Π in 1D domains can be performed by means of the Fast Marching Method (as proposed in [12]).

B. Characteristics of E_{MSN} as a shape metric

Energy E_{MSN} quantifies differences between shapes through their geometric features as it constitutes a metric in shape space as defined in [13]. That is, considering three shapes γ_1, γ_2 and γ_3:

$$\begin{aligned} E_{\mathrm{MSN}}(\gamma_1,\gamma_2) &= E_{\mathrm{MSN}}(\gamma_2,\gamma_1), \\ E_{\mathrm{MSN}}(\gamma_1,\gamma_2) = 0 &\Rightarrow \gamma_1 \equiv \gamma_2, \\ E_{\mathrm{MSN}}(\gamma_1,\gamma_3) &\leq E_{\mathrm{MSN}}(\gamma_1,\gamma_2) + E_{\mathrm{MSN}}(\gamma_2,\gamma_3). \end{aligned} \tag{4}$$

Some relevant features of metric E_{MSN} for OCSC are:

*1) **Invariance to SE(2):*** E_{MSN} decouples rigid motions from shape-defining characteristics. Our analysis is performed from local frames $\Re(s)$ (and $\bar{\Re}(\bar{s})$) thus making errors (2) locally invariant to SE(2) and energy (3) globally invariant to SE(2). In the literature, a common approach for ensuring SE(2) invariance involves using the Procrustes rigid transform [6], [13], [14]. However, a global rigid adjustment of the target shape may increment local errors for which no corrective action can be taken (deformable objects can be highly under-actuated).

*2) **Multi-scale scope:*** Given an unfeasible target shape (conditioned by both the deformation properties of the object and the configuration of the grippers), a multi-scale analysis allows the error reduction of geometric features appearing at larger scales, while simultaneously preserving local geometric features.

*3) **Use of elastic mapping:*** Geometry-preserving elastic maps favour shape evolution paths of lower deformation. Conventional approaches such as [6] or [7] use homogeneous mappings between contours and thus assume isometric deformations (i.e., stretching/compressing processes are assumed to be negligible). When dealing with non-isometric deformations, homogeneous mappings define errors that generate larger deformation paths (i.e., deviations that may even affect the feasibility of the task).

*4) **Joint intrinsic-extrinsic metric:*** E_{MSN} is intrinsic, since it is defined by geodesic distances and local coordinates, and extrinsic, as it is based on the multi-scale mean normal curvature obtained from the extrinsic analysis of domains $B(s,r)$. In shape control, a conventional approach is to minimise extrinsic energies that disregard the object's topology. The joint intrinsic-extrinsic nature of E_{MSN} makes it aware of topology changes and non-isometric deformations [8] leading to gentler deformation paths.

C. Extrinsically-defined shape energies

In this section, we revisit general definitions of the conventional extrinsic shape energies E_{P2P}, used in [6], [9], [12], [15] or [16], and E_{FT}, used in [7]. We endow them with elastic maps in order to fairly compare their performance with our proposed energy E_{MSN} in upcoming sections.

The point-to-point (P2P) error, endowed with an elastic map Π, can be formulated as:

$$\mathbf{e}_{\mathrm{P2P}}(s,t) = \mathbf{x}(s,t) - (\mathbf{R}^* \bar{\mathbf{x}}(\Pi(s,t)) + \mathbf{t}^*), \tag{5}$$

where $\mathbf{x}(s,t), \bar{\mathbf{x}}(\Pi(s,t)) \in \mathbb{R}^2$ are the extrinsic coordinates of the current and target contour points respectively. Transform $(\mathbf{R}^*, \mathbf{t}^*)$ is the orthogonal Procrustes rigid transform [13] that, by removing the rigid translation and rotation component from the point-to-point error, minimises the energy:

$$E_{\mathrm{P2P}}(\gamma(t),\bar{\gamma}) = \min_{\mathbf{R}^*, \mathbf{t}^*, \Pi} \int_0^{l(t)} \mathbf{e}_{\mathrm{P2P}}^\intercal \mathbf{e}_{\mathrm{P2P}} \mathrm{d}s. \tag{6}$$

Alternatively, energy E_{FT} is defined in the frequency domain through the Fourier Transform. Consider the complex function $z(s) = x(s) + y(s)i$, where the $x(s)$ coordinates of $\gamma(s)$ constitute the real term and the $y(s)$ coordinates the imaginary term. The complex Fourier coefficients $c_n, \bar{c}_n$ obtained from $z(s), \bar{z}(\Pi(s))$ lead to the Fourier-based energy:

$$E_{\mathrm{FT}}(\gamma(t),\bar{\gamma}) = \min_{\Pi} \sum_{n=-\infty}^{\infty} |c_n - \bar{c}_n|^2. \tag{7}$$

Note that the summation bounds in (7) can be truncated thus allowing to filter out high frequency (nosiy) components.

Lemma II.1. *Shape energies E_{P2P} and E_{FT}, defined in (6) and (7) respectively, are equivalent (up to a Procrustes transform).*

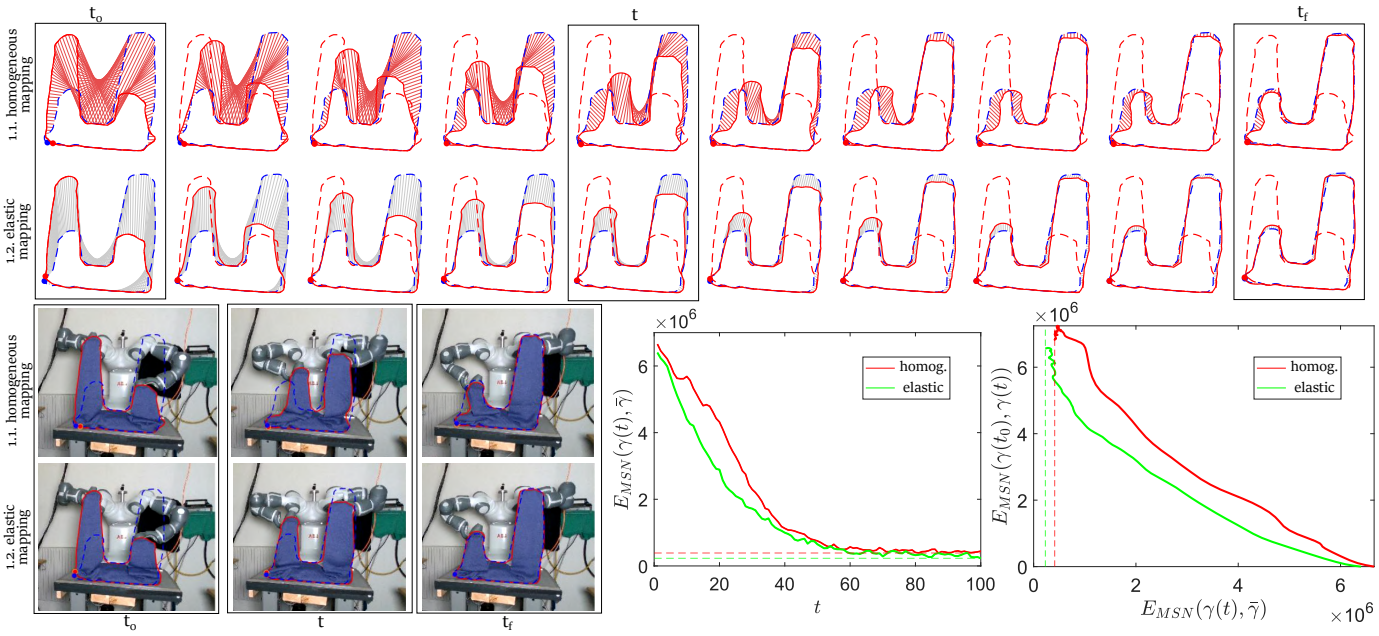

Fig. 3. Two experiments involving the manipulation of a sweater. Both solve the same shape control problem by reducing the shapes' Fourier-based spectral energy. Experiment 1.1 makes use of homogeneous contour mapping whereas Exp. 1.2 uses an elastic mapping that considers resemblance of local geometric features (i.e., E_{FT} in (7)). The results are analysed through E_{MSN} to validate it as a deformation measure. On the top, the initial shape state $\gamma(s,t_0)$ (red dashed line), the shape evolution $\gamma(t)$ (red line) and the target shape $\bar{\gamma}$ (blue dashed line) are shown with the contour maps: thin lines linking the contours in red for the homogeneous map (Exp. 1.1) and in gray for the elastic map $\Pi(s,t)$ (Exp. 1.2). Three relevant frames per experiment are shown (bottom left), corresponding to the time moments framed in black rectangles on the top sequences. First plot on the bottom (centred) shows the evolution of the shape error expressed in terms of $E_{\mathrm{MSN}}(\gamma(t),\bar{\gamma})$. Second plot (bottom right) shows the evolution of the deformation cost $E_{\mathrm{MSN}}(\gamma(t_0),\gamma(t))$ with respect to the shape error $E_{\mathrm{MSN}}(\gamma(t),\bar{\gamma})$. In both plots, the minimum achieved error values are plotted with dashed lines. Metric E_{MSN} properly represents the shape error evolution and the deformation path followed by each process. The homogeneous map deviates the shape evolution in Exp. 1.1 towards a higher deformation path (left sleeve folds inconveniently), thus hindering convergence to the desired shape. Cost $E_{\mathrm{MSN}}(\gamma(t_0),\gamma(t))$ reflects this fact: the red line lies above the green line throughout the whole error evolution (second plot).

Proof. The proof follows from the direct application of Parseval's Theorem [17] to (7):

$$\sum_{n=-\infty}^{\infty} |c_n-\bar{c}_n|^2 = \int_0^{l(t)} |z(s)-\bar{z}(\Pi(s))|^2\,\mathrm{d}s$$
$$= \int_0^{l(t)} \|\mathbf{x}(s)-\bar{\mathbf{x}}(\Pi(s))\|^2\mathrm{d}s = \int_0^{l(t)} \mathbf{e}_{\mathrm{P2P}}^{\mathsf{T}}\mathbf{e}_{\mathrm{P2P}}\mathrm{d}s. \quad (8)$$

D. Validation of E_{MSN} for OCSC

In this section we validate E_{MSN}, through experiments and simulations, as a metric that allows to quantify deformation and as a shape error that produces lower deformation paths in shape control.

The experiments presented along this paper are performed on the ABB Yumi dual-arm robot using colour-based object segmentation (in CIELAB colour space) and α-shape contour extraction. The continuous elastic contour map $\Pi(s,t)$ is computed as in [12] and then sampled to interpolate values of $\bar{\mathbf{I}}(\bar{s},r)$ in (2) with sub-pixel resolution. We avoid using any specific Jacobian update-rules (as in [5] or [7]) in order to compare the different energies as consistently as possible: Jacobians are experimentally estimated throughout the whole process in all the experiments.

To illustrate the performance of E_{MSN} as a deformation measure, we use it to analyse the results of experiments 1.1 and 1.2 (Fig. 3). Both experiments involve the reduction of the shapes' Fourier-based spectral energy. However, Exp. 1.1 uses a homogeneous contour mapping, whereas Exp. 1.2 uses elastic mapping (i.e., E_{FT} in (7)). As expected, the homogeneous mapping in Exp. 1.1 generates a larger deformation process. The proposed E_{MSN}, used to analyse the results, properly identifies such deviation.

Given lemma II.1, either E_{P2P} in (6) or E_{FT} in (7) serve to illustrate the importance of E_{MSN} being an intrinsic and extrinsic metric for OCSC. In order to provide a better insight on the characteristics of E_{MSN} as object-compliant shape metric, a comparison between two simulations is illustrated in Fig. 4. The first simulation seeks to reduce the extrinsic energy $E_{\mathrm{P2P}}(\gamma(t),\bar{\gamma})$ whereas the second simulation reduces $E_{\mathrm{MSN}}(\gamma(t),\bar{\gamma})$. The control strategy based on the reduction of E_{MSN} leads to lower measured deformation as illustrated in the plots of Fig. 4. Moreover, the deformation cost expressed in terms of $E_{\mathrm{MSN}}(\gamma(t_0),\gamma(t))$ is representative of the deformation values obtained from the simulation (unlike deformation cost expressed as $E_{\mathrm{P2P}}(\gamma(t_0),\gamma(t))$).

To further illustrate how our shape metric $E_{\mathrm{MSN}}(\gamma(t),\bar{\gamma})$ inherently reduces not only the compression/extension strain but also the bending processes, in Fig. 5 we present Exp. 2.1 and Exp. 2.2. They involve the manipulation of an Ethernet cable that cannot be stretched or compressed (pure isometric deformations). Strategies based on the reduction of $E_{\mathrm{P2P}}(\gamma(t),\bar{\gamma})$ and $E_{\mathrm{MSN}}(\gamma(t),\bar{\gamma})$ are compared again in Exp. 2.1 and Exp. 2.2 respectively. This particular shape

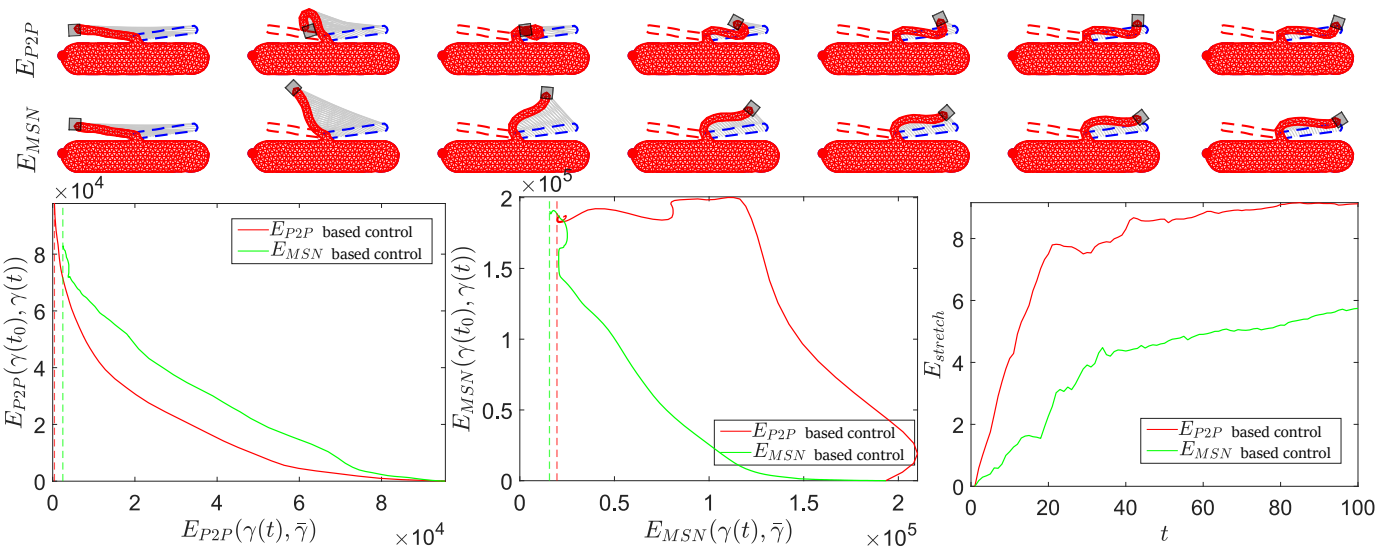

Fig. 4. Two simulations illustrate the performance of E_{MSN} as shape error and deformation cost. A shape control problem is solved using two strategies, one reduces $E_{\mathrm{P2P}}(\gamma(t),\bar{\gamma})$, the other $E_{\mathrm{MSN}}(\gamma(t),\bar{\gamma})$. On the top sequences, the simulation deformation mesh (red triangles) and the gripper (black square) are shown along with other elements introduced in the description of Fig. 3. On the bottom, three plots illustrate the performance of E_{MSN} as deformation energy by comparing it to the purely extrinsic energy E_{P2P}. The first plot shows, for both control strategies, the deformation path that shapes follow according to E_{P2P}, i.e., it plots deformation cost $E_{\mathrm{P2P}}(\gamma(t_0),\gamma(t))$ with respect to shape error $E_{\mathrm{P2P}}(\gamma(t),\bar{\gamma})$ (the E_{MSN} based control, in green, leads to a larger cost path). The plot in the middle shows the deformation path in terms of E_{MSN} (the E_{MSN} based control, in green, leads to a significantly lower deformation path). The third plot validates the information provided by the E_{MSN}-based analysis by showing the evolution of the actual deformation with respect to time. That is, the stretch measured in the simulation (computed as the sum of the absolute value of length variations on the mesh's segments) is significantly larger on the strategy that reduces E_{P2P}.

control problem constitutes a clear example of how seeking a local minimum in extrinsic energies such as $E_{\mathrm{P2P}}(\gamma(t),\bar{\gamma})$ can lead to very large deformation processes that may even result in object self-intersections. See the high deformation and self-intersection of the cable in Exp. 2.1. On the other hand, the joint nature of $E_{\mathrm{MSN}}(\gamma(t),\bar{\gamma})$ allows to *untangle* the cable and achieve a proper solution in Exp. 2.2. In Exp. 2.2 the intrinsic nature of the E_{MSN} (SE(2) invariant) seeks to match the target contour's curvature regardless of its rigid configuration (position and orientation). That is, the strategy in Exp. 2.2 seeks object shape control rather than object position control, as Exp. 2.1 does.

III. OCSC FRAMEWORK

The use of $E_{\mathrm{MSN}}(\gamma(t),\bar{\gamma})$ as shape error favours object-compliant behaviour of the shape control system. However, some applications may require further penalising the amount of deformation during the control process in order to limit specific object configurations. The multi-scale definition of E_{MSN} and the information enclosed in the elastic map Π allow for the object-compliant analysis to be taken further, we develop and exploit both concepts in this section.

A. Object-compliant energy: E_{OC}

E_{MSN} energy can be used to formulate both shape error $E_{\mathrm{MSN}}(\gamma(t),\bar{\gamma})$ and deformation cost $E_{\mathrm{MSN}}(\gamma(t_0),\gamma(t))$. One may suggest combining both in a shape control strategy that seeks reducing an object-compliant (OC) energy:

$$E_{\mathrm{OC}}(\gamma(t),\bar{\gamma}) = E_{\mathrm{MSN}}(\gamma(t),\bar{\gamma}) + \beta E_{\mathrm{MSN}}(\gamma(t_0),\gamma(t)), \quad (9)$$

where parameter $\beta \geq 0$ allows to weigh the deformation cost with respect to the shape error of the control task. Equation (9) constitutes the projection of two optimisation functions onto a single one E_{OC}. Since both cost functions are defined through the same metric E_{MSN}, (9) can be also regarded as shape-evolution path (parameterised by β) in the shape space defined by the shape representation (1). This feature means that establishing a specific value of β in (9) is equivalent to defining an new target shape γ_β in-between $\gamma(t_0)$ and $\bar{\gamma}$, resulting from an interpolation in the shape representation space defined by (1). With these considerations (9) can be expressed as:

$$E_{\mathrm{OC}}(\gamma(t),\bar{\gamma}) = E_{\mathrm{MSN}}(\gamma(t),\gamma_\beta). \quad (10)$$

The major issue with (10) is that it does not consider *per se* how the object is deforming, but rather defining a closer reference γ_β in shape space. One could try to highly penalise deforming away from $\gamma(t_0)$ by establishing very high values of β in (9). That would lead to re-defining a target shape γ_β in the neighbourhood of $\gamma(t_0)$ (locally in shape space). Very close-by target shapes γ_β might imply a worse performance in shape control tasks. On the other hand, if we relax the deformation cost and establish low values of β, the obtained reference shapes γ_β still do not guarantee an object-compliant shape evolution path towards $\bar{\gamma}$.

For this reason, we propose to exploit the multi-scale nature of E_{MSN} and define the following object-compliant energy:

$$E_{\mathrm{OC}}(\gamma(t),\bar{\gamma}) = E_{\mathrm{MSN}}(\gamma(t),\bar{\gamma}) + \beta \min_{\Pi} \int_0^{l(t)} \int_0^{r_{\mathrm{OC}}} \|\mathbf{l}(s,r,t) - \mathbf{l}(\Pi(s,t),r,t_0)\|^2 \mathrm{d}r\mathrm{d}s, \quad (11)$$

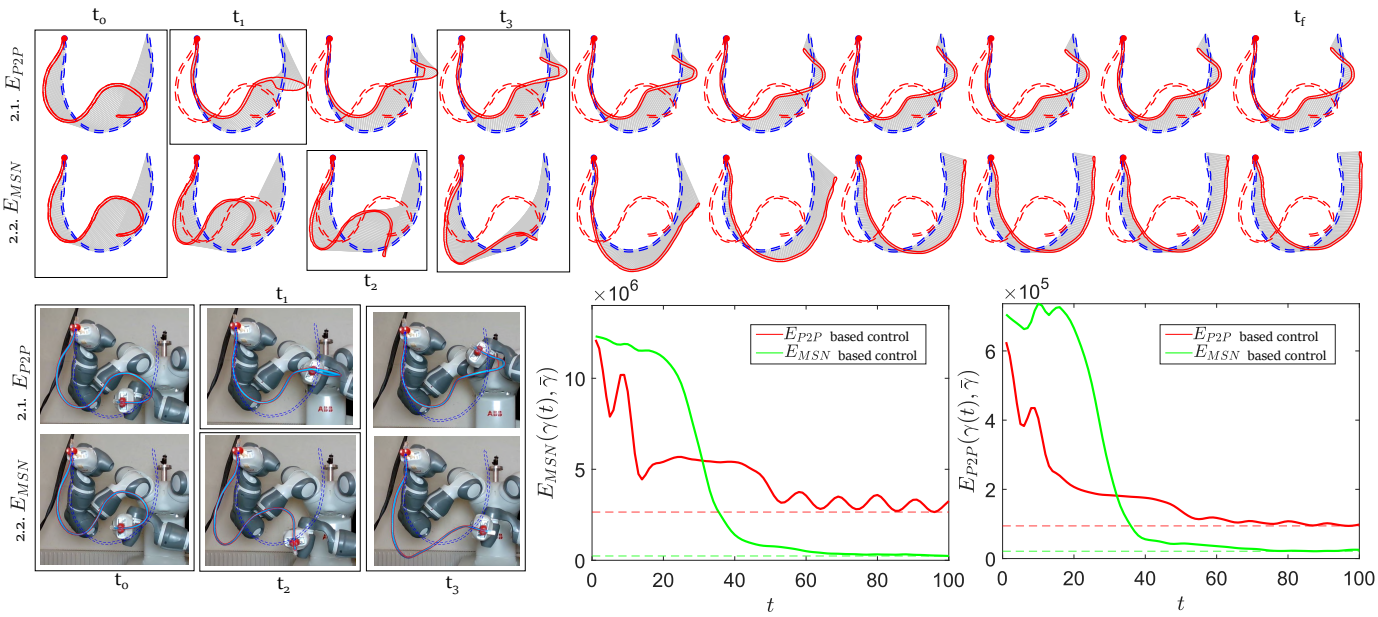

Fig. 5. Two experiments illustrate the importance of the joint nature (both intrinsic and extrinsic) of $E_{\mathrm{MSN}}(\gamma(t),\bar{\gamma})$ with respect to extrinsic energies such as $E_{\mathrm{P2P}}(\gamma(t),\bar{\gamma})$. An Ethernet cable that can only be deformed isometrically needs to be *untangled* in order to achieve the shape control task (gripper on the left is fixed). Control laws in experiments 2.1 and 2.2 seek reducing $E_{\mathrm{P2P}}(\gamma(t),\bar{\gamma})$ and $E_{\mathrm{MSN}}(\gamma(t),\bar{\gamma})$ (respectively). Elements of the shape sequences (and the video frames) are introduced in the description of Fig. 3. For both experiments, the first plot (centre) shows the evolution of $E_{\mathrm{MSN}}(\gamma(t),\bar{\gamma})$ and the second plot (right) shows the evolution of $E_{\mathrm{P2P}}(\gamma(t),\bar{\gamma})$. Reduction of E_{P2P} (extrinsic) in Exp. 2.1 pursues a local minimum that leads to twisting the cable thus leading to large deformations, oscillations and self-occlusions that hinder the control process. Reducing E_{MSN} in Exp. 2.2 allows to *untangle* the cable and achieve a proper final shape. The evolution of the E_{P2P} energy of Exp. 2.2 (green plot on the right) shows the need of *escaping* a local minimum, i.e., temporarily increasing energy E_{P2P}.

where the deformation cost (second term) is defined within a specific scale range $r \in (0, r_{\mathrm{OC}}]$ (being $0 < r_{\mathrm{OC}} \leq r_{\max}$). As the scale value $r_{\mathrm{OC}} \to 0$, the second term in the right hand side of (11) becomes negligible thus (11) turns equivalent to (3). On the other hand, if $r_{\mathrm{OC}} = r_{\max}$, (11) is equivalent to (9). That is, rather than disregarding the deformation cost in the formulation (as (3) does) or defining a specific intermediate shape state between two shapes like (9), the object-compliant energy E_{OC} in (11) penalises changes in length and curvature on a specifically targeted range of scales.

This formulation allows to establish high penalisation values to the deformation cost (i.e., establish very high values for β) while not over-constraining the set of low deformation paths. If the target shape $\bar{\gamma}$ is within (or nearby) any of the shape evolution paths defined by (11), deformations can be highly penalised while still allowing to significantly reduce the shape control error. The choice of r_{OC} is closely related to the rigidness of the deformable object. If the object does not present a very high rigidness (e.g., a chewing gum), r_{OC} can take very low values whereas objects with higher rigidness (e.g., a cardboard piece) will benefit from higher r_{OC} values that penalise large changes in both local and larger-scale curvatures.

B. Elastic mapping based strain limits

A global strain measure could be approximated through the change in the total length of the object $e(t) = l(t)/l(t_0)$. However, strain $e(t)$ does not provide a reliable measure when deformations are unevenly distributed over the object. We therefore require a local measure of the strain that allows to detect strain limits being reached in specific object parts.

Under the assumption of isotropic behaviour, we propose characterising the object's local strain through the evolution of the elastic map Π_ϵ defined between its current state $\gamma(t)$ and its initial state $\gamma(t_0)$:

$$\Pi_\epsilon = \arg\min_{\Pi_\epsilon} \int_0^{l(t)} \int_0^{r_{\max}} \|\mathbf{l}(s,r,t) - \mathbf{l}(\Pi_\epsilon(s,t),r,t_0)\|^2 \mathrm{d}r\mathrm{d}s. \tag{12}$$

That is, we approximate the local strain $\epsilon(s,t)$ as:

$$\epsilon(s,t) \approx \left.\frac{\partial \Pi_\epsilon(s,t)}{\partial s}\right|_t. \tag{13}$$

Partial derivative $\partial\Pi_\epsilon(s,t)/\partial s$ provides a measure of local change in the relative density of the object (with respect to its density at t_0). If $\epsilon(s,t) = 1$ the object mass distribution at point s is the same as in the initial time instant. On the other hand, if $\epsilon(s,t) > 1$ or $\epsilon(s,t) < 1$ the object has been respectively stretched or compressed at s, respectively.

IV. Experiments

The first group of experiments (Fig. 6) compares the performance of a Jacobian-based control law applied to four different energies, particularly $E_{\mathrm{P2P}}, E_{\mathrm{FT}}, E_{\mathrm{MSN}}$ and E_{OC} (Exp. 3.1 to 3.4, respectively). The extrinsic shape energies E_{FT} and E_{P2P} lead to larger deformation paths (i.e., equivalent paths, lemma II.1), whereas the strategy that seeks reducing E_{OC} leads to lower deformation. Note time instant t_1 where, if instead of cloth a thin metal sheet was being deformed, E_{MSN}

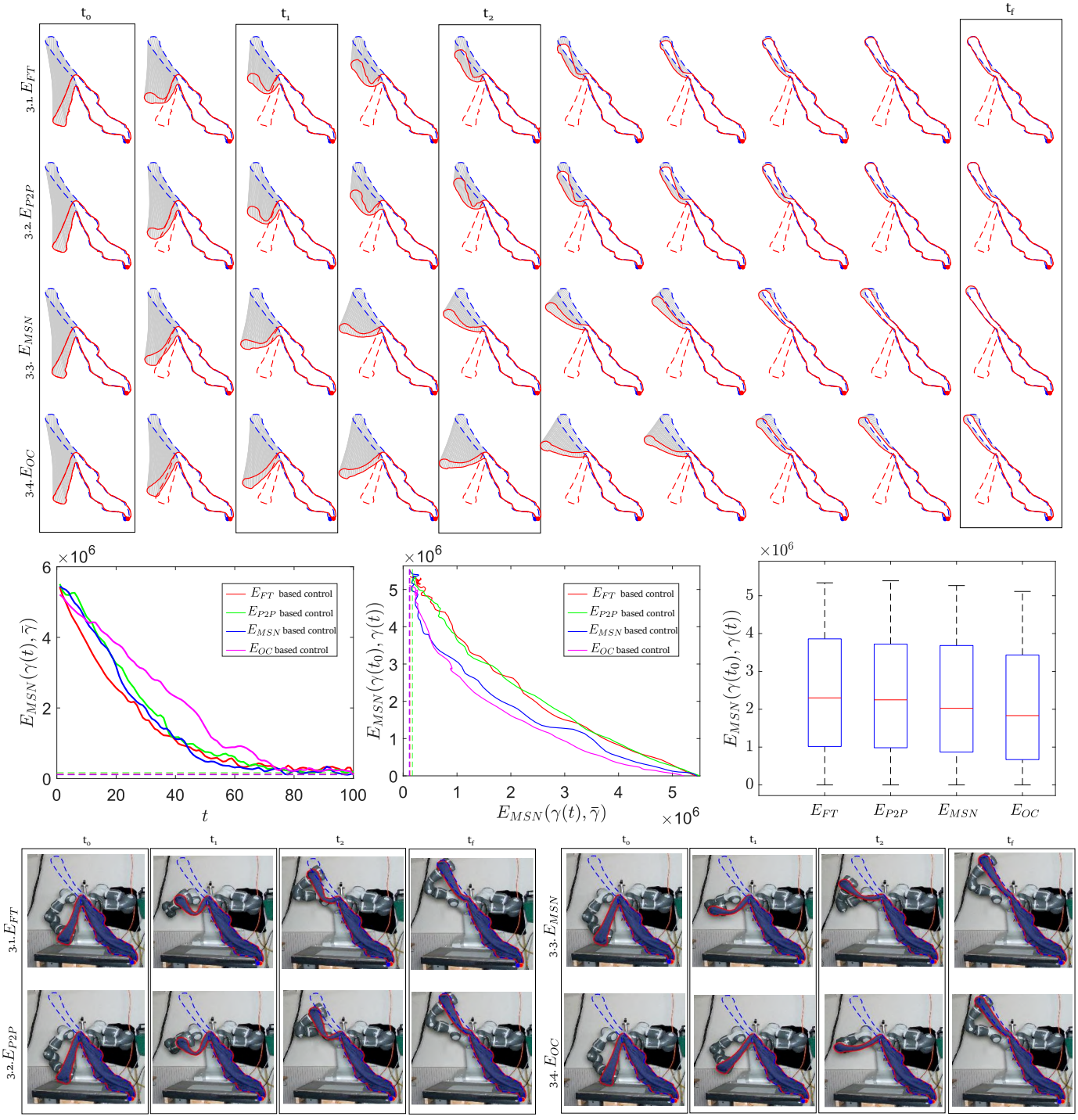

Fig. 6. Four experiments involve shape control of a sweater (right gripper is fixed). The object-compliant performance of four shape control strategies is compared, reducing respectively E_{FT} (Exp. 3.1), E_{P2P} (Exp. 3.2), E_{MSN} (Exp. 3.3) and E_{OC} (Exp. 3.4). Experiment 3.4 reduces E_{OC} (11) with $\beta = 1$ and $r_{\mathrm{OC}} = 0.1 r_{\max}$ thus penalising relatively local deformations. Elements in graphs and plots are introduced in the description of Fig. 3 except for the box-plot on the right, which represents the deformation cost distribution of each strategy according to $E_{\mathrm{MSN}}(\gamma(t_0), \gamma(t))$. First plot (left) shows how all strategies lead to similar final absolute error values. In the middle plot, Exp. 3.4 leads to the lowest deformation path (purple line). This is shown in the shape evolution sequences (above), where Exp. 3.4 generates almost no changes in the local curvature of the shape besides the bending in the pivoting region (centre of the object). The equivalence of E_{P2P} and E_{FT} (lemma II.1) is exemplified in Exp. 3.1 and Exp. 3.2: both extrinsic energies follow similar shape evolution paths (middle plot), generate large deformations and, unlike Exp. 3.3 and Exp. 3.4, lead to curvature error in the middle part of the object (see the t_f instants above).

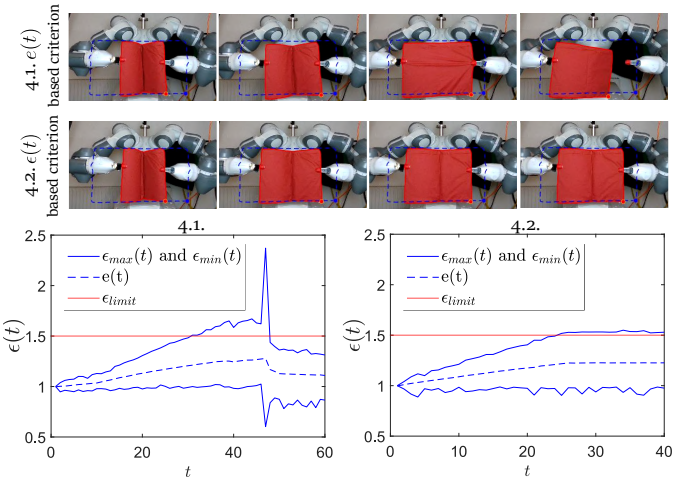

Fig. 7. Stretching process of a cardboard piece towards an unfeasible target shape that requires over-stretching the object. In the plots, average values $\epsilon_{avg}(t) \equiv e(t)$, maximum $\epsilon_{max}(t)$ and minimum $\epsilon_{min}(t)$ values of $\epsilon(s,t)$ with respect to s are plotted, hence the dependence on s has been removed from the y-axis label. The system receives as input the strain limit of $\epsilon_{limit} = 1.5$. In Exp. 4.1 the strain is measured through e(t) whereas in Exp. 4.2 $\epsilon(t)$ is used as local strain measure. This task involves unevenly distributed contour length changes: vertical sides of the shape do not change their length. In Exp. 4.1, Strain measure $e(t)$ does not perceive the limit $\epsilon_{limit} = 1.5$ being reached, thus the object is over-stretched leading to grip failure: note the abrupt change in plot 4.1 (around second 45). Local strain measure $\epsilon_{max}(t)$ in Exp. 4.2 allows to stop the control when the strain limit is reached. Note that $\epsilon(t)$ also allows (through $\epsilon_{min}(t)$) to consider the maximum local compression that takes place on the object.

would likely lead to high compression and higher chances of bucking, whereas E_{OC} generates a less aggressive shape evolution. In experiment 3.4, the solution trajectory of the robot arm performs a longer circular arch, thus leading to a slightly slower performance. Further analysis is presented in the description of Fig. 6. Experiments 4.1 and 4.2 in Fig. 7 illustrate the performance of (13) as an approximation of a local strain measure. They compare $e(t)$ (Exp. 4.1) and $\epsilon(t)$ (Exp. 4.2) as approximations of an object's strain (with strain limit 1.5 as input information). Measure $e(t)$ leads to an over-stretching action that causes gripper failure. On the other hand, $\epsilon(t)$ allows to properly stop the process thus preventing failure (see description on Fig. 7 for more insights).

V. Conclusions

We introduced a contour-based shape metric and a framework for vision-based OCSC with focus on texture-less objects. Experiments that validate the approach illustrate how energy E_{MSN} achieves a balance between reducing the amount of deformation and faster performance, while E_{OC} enables more conservative (less aggressive) shape evolutions but presents a slightly slower performance. Some interesting future research lines include testing the performance of E_{MSN} on 3D contour data, thus allowing to define target shapes in more detail. However, regardless of 2D or 3D contour data being used, there may be cases where the visual contour does not change significantly. For instance, the object may be undergoing large deformations that cannot be noticed (e.g. a bulging object). This problem could be tackled by extending the method for the analysis of surfaces (rather than contours), with the main challenges being the computation of elastic maps between surfaces as well as the surface parameterisation and the definition of the local frames of reference $\Re(s)$. Another avenue is to investigate how force information obtained from force sensors on the manipulators [18] can complement E_{OC}.

References

[1] P Jiménez. Survey on model-based manipulation planning of deformable objects. *Robotics and computer-integrated manufacturing*, 28(2):154–163, 2012.

[2] R. Herguedas, G. López-Nicolás, R. Aragüés, and C. Sagüés. Survey on multi-robot manipulation of deformable objects. In *24th IEEE International Conference on Emerging Technologies and Factory Automation*, pages 977–984, 2019.

[3] D. Navarro-Alarcon, H.M. Yip, Z. Wang, Y.H. Liu, F. Zhong, T. Zhang, and P. Li. Automatic 3-D manipulation of soft objects by robotic arms with an adaptive deformation model. *IEEE Transactions on Robotics*, 32(2):429–441, 2016.

[4] D. Navarro-Alarcón, Y. Liu, J.G. Romero, and P. Li. Model-free visually servoed deformation control of elastic objects by robot manipulators. *IEEE Transactions on Robotics*, 29(6):1457–1468, 2013.

[5] J. Zhu, D. Navarro-Alarcon, R. Passama, and A. Cherubini. Vision-based manipulation of deformable and rigid objects using subspace projections of 2-D contours. *Robotics and Autonomous Systems*, 142:103798, 2021.

[6] G. López-Nicolás, R. Herguedas, M. Aranda, and Y. Mezouar. Simultaneous shape control and transport with multiple robots. In *IEEE International Conference on Robotic Computing*, pages 218–225, 2020.

[7] D. Navarro-Alarcon and Y.H. Liu. Fourier-based shape servoing: a new feedback method to actively deform soft objects into desired 2-D image contours. *IEEE Transactions on Robotics*, 34(1):272–279, 2017.

[8] A. M Bronstein, M. M Bronstein, and R. Kimmel. Rock, paper, and scissors: extrinsic vs. intrinsic similarity of non-rigid shapes. In *IEEE 11th International Conference on Computer Vision*, pages 1–6, 2007.

[9] D. Berenson. Manipulation of deformable objects without modeling and simulating deformation. In *IEEE/RSJ International Conference on Intelligent Robots and Systems*, pages 4525–4532, 2013.

[10] M. Ruan, D. McConachie, and D. Berenson. Accounting for directional rigidity and constraints in control for manipulation of deformable objects without physical simulation. In *IEEE/RSJ International Conference on Intelligent Robots and Systems*, pages 512–519, 2018.

[11] Z. Hu, P. Sun, and J. Pan. Three-dimensional deformable object manipulation using fast online Gaussian process regression. *IEEE Robotics and Automation Letters*, 3(2):979–986, 2018.

[12] I. Cuiral-Zueco and G. López-Nicolás. Multi-scale Laplacian-based FMM for shape control. In *IEEE/RSJ International Conference on Intelligent Robots and Systems*, pages 3792–3797, 2021.

[13] R. Al-Aifari, I. Daubechies, and Y. Lipman. Continuous procrustes distance between two surfaces. *Communications on Pure and Applied Mathematics*, 66(6):934–964, 2013.

[14] I. H. Jermyn, S. Kurtek, E. Klassen, and A. Srivastava. Elastic shape matching of parameterized surfaces using square root normal fields. In *European conference on computer vision*, pages 804–817, 2012.

[15] M. Shetab-Bushehri, M. Aranda, Y. Mezouar, and E. Ozgur. As-rigid-as-possible shape servoing. *IEEE Robotics and Automation Letters*, 7(2):3898–3905, 2022.

[16] M. Aranda, J.A. Corrales Ramon, Y. Mezouar, A. Bartoli, and E. Özgür. Monocular visual shape tracking and servoing for isometrically deforming objects. In *IEEE/RSJ International Conference on Intelligent Robots and Systems*, pages 7542–7549, 2020.

[17] M.A. Parseval. Mémoire sur les séries et sur l'intégration complète d'une équation aux différences partielles linéaires du second ordre, à coefficients constants. *Mém. prés. par divers savants, Acad. des Sciences, Paris,(1)*, 1:638–648, 1806.

[18] F. Süberkrüb, R. Laezza, and Y. Karayiannidis. Feel the tension: Manipulation of deformable linear objects in environments with fixtures using force information. In *IEEE/RSJ International Conference on Intelligent Robots and Systems*, pages 11216–11222, 2022.